

# Impact of $\text{Ni}(\text{OH})_2$ Platelike Particles on Lamellar Surfactant Mesophases and the Orientation of Their Mixtures under Elongational Flow

S. Junaid S. Qazi<sup>\*,†</sup> and Adrian R. Rennie

Materials Physics, Department of Physics and Astronomy, Uppsala University, Box 516, SE-751 20 Uppsala, Sweden

Ian Tucker

Unilever Research and Development, Port Sunlight Laboratory, Quarry Road East, Bebington, Wirral CH63 3JW, U.K.

Jeff Penfold

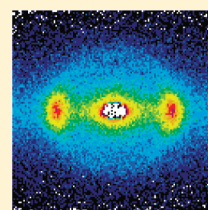
ISIS Facility, STFC, Rutherford Appleton Laboratory, Chilton, Didcot, Oxon OX11 0QX, U.K.

Isabelle Grillo

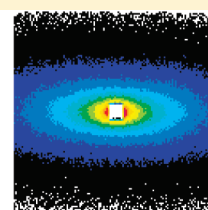
Institut Laue Langevin, F-38042 Grenoble, France

 Supporting Information

**ABSTRACT:** This article describes the behavior under elongational flow of mixtures of lamellar fragments and platelike colloidal particles. Mixtures of a dialkyl chain cationic surfactant, DHTAC (15 wt %), and the nonionic surfactant Brij 97 (0.5 wt %) form dispersions of lamellar phase fragments, and these were studied in the presence of smaller platelike colloidal particles of  $\text{Ni}(\text{OH})_2$  stabilized with sodium polyacrylate. Small-angle neutron scattering was used to follow the changes in the lamellar phase fragments in the mixture under elongational flow. The addition of a small fraction of the  $\text{Ni}(\text{OH})_2$  dispersion resulted in significantly increased viscosity and reduced the structure and size of the lamellar fragments, and this effect was further enhanced because of the flow induced alignment. The behavior of the mixture under elongational flow is described, and the induced orientation is discussed in terms of order parameters at the different positions using spatially resolved small-angle scattering. The effect of flow rate on the orientational alignment in the mixture is also described.



Lamellar fragments



Mixture of lamellar fragments and  $\text{Ni}(\text{OH})_2$  particles

## INTRODUCTION

Colloidal mixtures are interesting because of their rich rheological behavior and significant importance in industry. For example, clay minerals with cationic surfactants<sup>1</sup> have been studied because of their many applications such as in drilling fluids, paints, greases, inks, and cosmetic formulations. Protein-rich systems have been used to produce novel anisotropic food structures<sup>2</sup> by well-defined flow geometries and patterns. Formation of colloidal microstructures by flow processing<sup>3</sup> has particular importance in the food industry, where the control of alignment and order in all of these dispersions largely determine their properties. General aspects of rheological phenomenology are well-described in standard texts.<sup>4,5</sup> A significant focus is now on understanding the physical properties of materials in terms of their microscopic structure and the interactions of their components. Scattering techniques with light, X-rays, and neutrons have thus proved valuable in providing information about

the mesoscale structure as materials undergo deformation. Several articles and reviews provide a good background to research on shear of surfactant lamellar phases,<sup>6</sup> particulate colloidal dispersions,<sup>7</sup> and mixtures of different particles.<sup>8</sup> Structural changes studied by scattering are particularly emphasized in the review by Vermant and Solomon<sup>9</sup> that relates experimental studies of dispersions under shear with modeling. Platelike particles such as clays<sup>10</sup> and monodisperse hexagonal plates formed of nickel hydroxide<sup>11</sup> have also been studied under shear. These studies have highlighted the importance not just of the shape and size of colloidal particles but also of the interactions between the components in a dispersion. An example is the modeling of spherical particles and different interparticle forces to understand shear thickening behavior.<sup>12</sup>

**Received:** April 20, 2011

**Revised:** July 20, 2011

**Published:** July 22, 2011

Orientation of anisotropic particles such as rods and ellipsoids in shear flow has been the subject of several fluid mechanics calculations.<sup>13,14</sup> The particular case of disks was included in a study by Gauthier et al.,<sup>15</sup> although their experiments were performed on larger particles. More recent experiments have included microscopic examination of smaller ellipsoidal particles that exhibited significant Brownian motion.<sup>16</sup> Rods under extensional flow were discussed by Mewis and Metzner.<sup>17</sup>

Mixtures of particles with other particles, surfactants, and polymers have been studied extensively in order to understand the relation between their properties and their structure under external fields. Mixtures of cationic surfactants and silica nanoparticles have been used to stabilize emulsions,<sup>18</sup> and such emulsions are known as suspoemulsions.<sup>19</sup> A depletion interaction between a non-adsorbing polymer, polystyrene, and sterically stabilized latex of poly(methyl methacrylate) extensively modifies the phase behavior.<sup>20</sup> Clustering has been reported,<sup>21,22</sup> and the cluster size increases with increasing volume fraction of the colloid, resulting in large changes in rheological properties with increases in viscosity.

The assembly of cationic surfactants into micelles and other aggregates provides a range of interesting behaviors. Single-chain surfactants such as hexadecyltrimethylammonium bromide (CTAB) tend to form elongated micelles, particularly in the presence of large organic counterions that are slightly hydrophobic. The changes in viscosity of the micellar solutions with temperature and concentration can be interpreted in terms of the size and flexibility of the micelles.<sup>23</sup> More complicated systems such as mixtures of this surfactant with the biopolymer gelatin have also been studied.<sup>24</sup> Surfactants with two hydrophobic tails (gemini surfactants) can form micelles but have a marked tendency to produce lamellar phases. For example, dimethylene-1,2-bis(dodecyltrimethylammonium bromide)<sup>25</sup> with sodium salicylate counterions can produce highly ordered structures and solutions with high viscosity. For a gemini surfactant with longer hydrophobic groups such as erucyl bis-(hydroxyethyl) methylammonium chloride,<sup>26</sup> an increase in viscosity by a factor of more than  $10^7$  upon the addition of salt has been reported. The structural and shape changes in micellar aggregates that occur with varying composition have been used to explain the behavior of a mixture of cationic and anionic surfactants, CTAB and decylphosphoric acid, that showed shear thinning behavior with a viscosity plateau.<sup>27</sup> A shear induced transition from a lamellar phase to vesicles has been reported for a dichain cationic surfactant in water.<sup>28</sup>

Flow induced structures in colloidal dispersions are important in practical applications, and in these cases, geometries that do not cause simple uniform shear are of considerable interest. Some studies have involved pipe flow<sup>29–31</sup> of clay dispersions. There has been less focus on structural changes and orientation under elongational flow. Wormlike micelles formed from mixtures of the nonionic surfactant hexadecylhexa(oxyethylene glycol) ether ( $C_{16}EO_6$ ) with CTAB and the lamellar phase of  $C_{16}EO_6$  measured at 55 °C showed strong orientation under elongational flow<sup>32</sup> that was observed to increase with the flow rate. Mixtures of the dialkyl chain cationic surfactant 2,3-diheptadecylesterethoxy-*n*-propyl-1,1,1-trimethylammonium chloride (DHTAC) and the nonionic surfactants Brij 97 (an oleyl polyether with an average of 10 ethylene oxide units) and Coco20 (eicosaethylene glycol monododecyl ether) have also been studied under elongational flow and display similar trends of increased alignment with flow rate.<sup>33</sup> Mixtures of DHTAC and Brij 97 form stable

dispersions of lamellar phase fragments that can be considered as relatively large disklike particles.

The physical properties of various mixtures of colloidal particles and lamellar phase surfactants have attracted attention particularly regarding stability and phase behavior.<sup>34–39</sup> The materials chosen for this study were studied previously as pure components under elongational flow.<sup>33,40</sup> In the present experiments, we studied the effect of adding platelike colloidal particles formed from  $Ni(OH)_2$  to the lamellar phase fragments formed from mixtures of DHTAC and Brij 97 surfactants. In particular, we investigated the alignment in this mixture that is induced under conditions of elongational flow. Concentrated dispersions of  $Ni(OH)_2$  have been studied previously under elongational<sup>40</sup> and shear flow.<sup>11</sup> Dispersions of DHTAC/Brij 97 and  $Ni(OH)_2$  particles separately have shown orientational alignment under elongational flow as reported previously. The choice of the materials for study provides a model system and allows the previous results to be compared in this article with the ordering and other changes induced in their mixture. The lamellar phase and the mixture are both shear thinning, in a manner characteristic of many dispersions, and the results are related to the observed rheology.

## ■ SAMPLE PREPARATION AND RHEOLOGICAL MEASUREMENTS

**Preparation of Lamellar Fragments.** The cationic surfactant, DHTAC, was custom-synthesized and purified at Unilever Research (Bebington, Wirral, U.K.). Brij 97 was obtained from Sigma-Aldrich and recrystallized before use. The lamellar phase fragments were prepared by melting the surfactants and shear mixing through a small orifice with deoxygenated water as described in more detail elsewhere.<sup>41</sup> A mixture of 15 wt % DHTAC and 0.5 wt % of Brij 97 was prepared in  $D_2O$  and consisted predominantly of dispersed fragments of lamellar phase.<sup>42</sup> The weight-average hydrodynamic radius,  $R_h$ , of the lamellar fragments was found to be  $\sim 1200$  Å with a polydispersity index of 0.29, according to dynamic light scattering measurements.

**Preparation of  $Ni(OH)_2$  Particles.** Nickel(II) hydroxide particles, which are uniform hexagonal platelets, were prepared and sterically stabilized by adsorbing a sodium polyacrylate layer at their surfaces. Preparation followed the procedure reported by Brown et al.,<sup>43</sup> which uses controlled precipitation from a dilute aqueous solution of nickel(II) nitrate and ammonium hydroxide as originally proposed by Durand-Keklikian et al.<sup>44</sup> The average hydrodynamic radius,  $R_h$ , obtained from dynamic light scattering (DLS) was 450 Å with a polydispersity index of 0.22. The thickness of the adsorbed stabilizing polymer layer on the particle was estimated to be about 85 Å. Details of the characterization are described elsewhere.<sup>45</sup> After preparation, the stabilized sample was centrifuged and redispersed several times to replace the  $H_2O$  with  $D_2O$ . The estimated concentration of  $D_2O$  in the finally prepared sample was 97%.

**Preparation of Mixtures of Lamellar Fragments and  $Ni(OH)_2$  Particles.** The mixture studied under elongational flow was prepared by adding the dispersed nickel hydroxide particles to the lamellar fragment dispersion in the flow cell and allowing the two to mix under flow for a few minutes before starting the measurements. All samples were prepared by weight. The volume fractions were calculated assuming densities of 1.0 and  $3.93 \text{ g cm}^{-3}$  for the surfactant and the

nickel hydroxide, respectively. The sample studied under flow had a volume fraction of surfactant that forms the lamellar phase,  $f_L$ , of 0.12 and a volume fraction of nickel hydroxide particles,  $f_N$ , equal to 0.012. The remaining volume fraction in the sample was water to make the sum equal to unity. A separate series of samples was prepared to study the effects of changes in composition on the structure in which mixtures were prepared by keeping  $f_L$  constant at 0.12 and changing  $f_N$  from 0.002 to 0.012. D<sub>2</sub>O was used as the dispersion medium for samples under elongational flow to reduce the level of incoherent scattering, thus enabling measurements with a thicker sample path length. A few additional samples were measured in other mixtures of H<sub>2</sub>O and D<sub>2</sub>O to identify specific components of the structure in the mixtures.

**Rheological Measurements.** Dynamic viscosities were measured as a function of shear strain rate for the lamellar fragments at a volume fraction  $\sim 0.15$  and for the mixture of lamellar fragments and Ni(OH)<sub>2</sub> particles used in the scattering experiments under extensional flow. An AR 2000 rheometer with a parallel-plate geometry and a sample thickness of 0.25 mm was used and the samples were covered to avoid evaporation during measurements. Rheological measurements have shown decreases in viscosity with shear strain rate for both the lamellar fragments alone and the mixture with nickel hydroxide particles. The decrease is more pronounced in the dispersion of lamellar fragments, for which the viscosity changes from 1.4 Pa s at 50 s<sup>-1</sup> to 0.2 Pa s at 2000 s<sup>-1</sup> and then remains constant up to 10000 s<sup>-1</sup>. The decrease in viscosity for the mixture of lamellar phase fragments with particles was from 9.5 Pa s at 50 s<sup>-1</sup> to 0.2 Pa s at 6000 s<sup>-1</sup> and overlapped with that of the lamellar fragments alone at a constant value up to 10000 s<sup>-1</sup>. The viscosity of the mixture, after it had run continuously for one day during the scattering experiments under flow, was observed to be approximately one-half that measured four weeks later. It was also noticed that the viscosity of the mixtures increased with increasing concentration of Ni(OH)<sub>2</sub> particles.

The mixture used for the flow experiments with  $f_N$  equal to 0.012 was observed to be very viscous after six months. It looked more like a soft solid, and the viscosity was approximately 2–3 orders of magnitude higher than that measured after four weeks of the experiments. Often, solutions of cationic surfactants in water assemble into elongated micelles in the presence of salt, and the entanglements of these micelles causes significant increases in the viscosity of the solution.<sup>46</sup> Examples of this behavior have been seen with solutions of the cationic gemini surfactants dimethylene-1,2-bis(dodecyl-diethylammonium bromide),<sup>25</sup> hexadecyl trimethylammonium bromide,<sup>24</sup> and erucyl bis(hydroxyethyl) methylammonium chloride<sup>26</sup> that all increase in viscosity upon addition of salt. Although the DHTAC/Brij 97 sample used in the current study consisted mostly of lamellar fragments, a very small fraction of micelles was also present.<sup>42</sup> Growth of long micelles and aggregates of lamellar fragments in the presence of Ni(OH)<sub>2</sub> dispersion might lead to structural changes and entanglements that could cause an increase in the viscosity. Aggregates or elongated micelles could grow further with time, and the sample looked like a soft solid after six months. The average hydrodynamic radius,  $R_h$ , of the mixture was determined by dynamic light scattering to be 1400 Å. Further dynamic light scattering did not show a significant difference in the hydrodynamic radius of the lamellar fragments ( $R_h \approx 1200$  Å) and particles in the mixture four weeks after the experiments. However, it was very difficult to redisperse the mixture after six months, and large aggregates were observed.

## EXPERIMENTAL SECTION

Experiments were performed on the small-angle scattering instrument D22 at the Institut Laue Langevin, Grenoble, France. It is convenient to describe the intensity,  $I(Q)$ , as function of the momentum transfer,  $Q = (4\pi/\lambda) \sin(\theta/2)$ , where  $\lambda$  is the wavelength and  $\theta$  is the scattering angle. The distribution of scattered intensity was measured on a 1 m  $\times$  1 m two-dimensional position sensitive detector. Two different configurations were used: For measurements of the samples under flow, the detector was placed 10 m from the sample, and neutrons with a wavelength of 8 Å were used with a collimation distance of 11.2 m. The detector captures scattering for  $Q$  directions that lie in the vertical plane and covers azimuthal angles,  $\Phi$ , between 0 and  $2\pi$ . Measurements on static samples were made in 1 mm thick quartz cells, whereas the sample under elongational flow was measured in a specially designed opposed-jet flow cell.<sup>40</sup> The original design criteria of the crossed-slot elongational flow cell<sup>47</sup> were modified for neutron scattering, and the construction details of the cell are described elsewhere.<sup>32</sup> The cell was previously used to study the alignment of surfactant mesophases<sup>32,33</sup> and dispersions of Ni(OH)<sub>2</sub> particles<sup>40</sup> under elongational flow. Details of the experimental arrangement are similar to those described in our previous article.<sup>40</sup> A 1 mm diameter aperture was placed in front of the cell, and measurements were recorded at different positions in the flow field by scanning the cell across the beam in steps of 2 mm. The only major differences in the current experiments were that the thickness of the cell was 6 mm in the viewable quartz window of 20 mm diameter and the input and output flow channels had a cross-sectional area of 6  $\times$  10 mm. Separate measurements on samples at rest were made in 1 mm path length cells in a thermostatted sample changer at 25 °C. The wavelength was 6 Å, and the sample to detector distance was 17 m, so as to record data in the  $Q$  range from 0.003 to 0.044 Å<sup>-1</sup>. The observed fraction of the Ewald sphere is almost flat for small-angle scattering with long wavelength neutrons. The wavelength spread had a full-width half-maximum of 5%. The Bragg peaks from the lamellar structure of the surfactant phase could be observed readily in fully aligned samples in this study, as in the previous work.<sup>33</sup>

Measurements under elongational flow were made on the dispersion of lamellar fragments at the overall flow rate of 10 mL s<sup>-1</sup>. The mixture with the highest concentration of added Ni(OH)<sub>2</sub> ( $f_L = 0.12$ ,  $f_N = 0.012$ ) was measured at the three different flow rates 7, 13, and 28 mL s<sup>-1</sup>. The scattering patterns obtained at different positions in the cell for lamellar fragments alone are shown in Figure 3 (below), and those for the mixture with nickel hydroxide particles at the flow rate of 7 mL s<sup>-1</sup> are shown in Figure 4 (below). The scattering patterns for the mixture at the other flow rates are presented in Figure S1 in the Supporting Information.

## ESTIMATE OF EXTENSIONAL STRAIN RATE

The extensional strain rates for the measured flow rates were estimated from the flow patterns calculated using a finite-element computation package<sup>48</sup> that simulated the elongational flow cell. The simulation assumed a Newtonian fluid with a dynamic viscosity of 0.2 Pa s, as measured for both the lamellar fragments and the mixture with nickel hydroxide particles at a shear rate of 4000 s<sup>-1</sup>, and the density was taken as 1.1 g cm<sup>-3</sup>. Details of the simulation are described in our previous article.<sup>40</sup> The sample path length was 6 mm in the current studies. The average flow velocities for the inlet and outlet were calculated from the overall



flow rate. The estimated flow velocity at each inlet and outlet for the pure lamellar fragments sample was  $0.083 \text{ m s}^{-1}$ , and for the mixture at the three measured flow rates of 7, 13, and  $28 \text{ mL s}^{-1}$ , they were 0.058, 0.11, and  $0.23 \text{ m s}^{-1}$  respectively. These values correspond to one-half the overall volume flow rate, as there were two inlets and two outlets for the flow cell. The evaluation of the local velocity in the flow cell, calculated from the simulations, allowed for the estimation of the extensional strain rate,  $dv/dZ$ . The simulations showed that the extensional strain rate, for a given flow rate, increases in a region of less than 0.5 mm at the center of the cell and then remains approximately constant up to the outlet. The calculated value of the average extensional strain rate along the vertical axis for measurements with lamellar fragments at the flow rate of  $10 \text{ mL s}^{-1}$  is  $6.2 \text{ s}^{-1}$ , and for the mixture measured at the flow rates 7, 13, and  $28 \text{ mL s}^{-1}$ , the average extensional strain rates are 4.3, 8.2, and  $17 \text{ s}^{-1}$ , respectively. Because of the finite spatial resolution of the numerical simulations, local velocities were averaged over regions of 1 mm perpendicular to the flow for the strain rate calculations. These strain rates can be used to estimate the Peclet number,  $Pe$ , associated with the flow. This is usually taken as the ratio of energy per particle associated with the shear strain to the thermal energy and is defined as

$$Pe = 6\pi\eta_s a^3 \dot{\gamma} / k_B T \quad (1)$$

where  $\eta_s$  is the shear viscosity,  $a$  is a characteristic dimension such as the size or the separation of particle in the fluid,  $\dot{\gamma}$  is the shear strain rate,  $k_B$  is the Boltzmann constant, and  $T$  is the absolute temperature. For non-interacting particles, an alternative rotational Peclet number defined as the ratio of the shear strain rate to the rotational diffusion constant is sometimes considered.<sup>49</sup> This differs from  $Pe$  used here by a small numerical factor that depends on the shape and on the precise way that the characteristic dimension,  $a$ , is defined. If  $Pe$  is greater than 1, then the shear strain energies will be larger than the thermal energies and the particles could be aligned. In case of elongational flow, the shear viscosity  $\eta_s$  and the shear strain rates  $\dot{\gamma}$  in eq 1 are replaced by the elongational viscosity,  $\eta_l$ , and the elongational shear strain,  $\dot{\epsilon}$ , respectively.<sup>40</sup> As in other studies,<sup>16</sup> to make simple comparisons, the Peclet numbers were calculated with the zero shear viscosity. Trouton's rule<sup>50</sup> suggests that, for uniaxial strain of a Newtonian fluid  $\eta_l = 3\eta_s$ . Assuming that  $a$  is the diameter of the lamellar fragment, then the elongational Peclet number is in the approximate range of 10–50 for the samples studied. These values provide some guidance as to the possibility of alignment under flow but cannot account fully for the effects of strains in a complex flow geometry.

## EVALUATION OF ANISOTROPY IN THE SCATTERING PATTERNS UNDER FLOW

Preferentially aligned particles give rise to anisotropy in diffraction that comes from internal structure, as well as anisotropy in the small-angle scattering that arises from the shape and orientation of the anisotropic particles. The extent of alignment of the particles can be quantified from the distribution of the scattered intensity. Even Legendre polynomials<sup>30,51</sup> can be used to describe the intensity distribution with respect to the azimuthal angle  $\Phi$  at a given momentum transfer,  $Q$ . Theoretical models of the alignment of anisotropic particles describe the extent of orientation in terms of order parameters defined by Legendre polynomials,  $P_n(\cos \Phi)$ , where the first even polynomial is<sup>52</sup>  $P_2 = (3 \cos^2 \Phi - 1)/2$ . An order parameter,  $S_2$ , can be

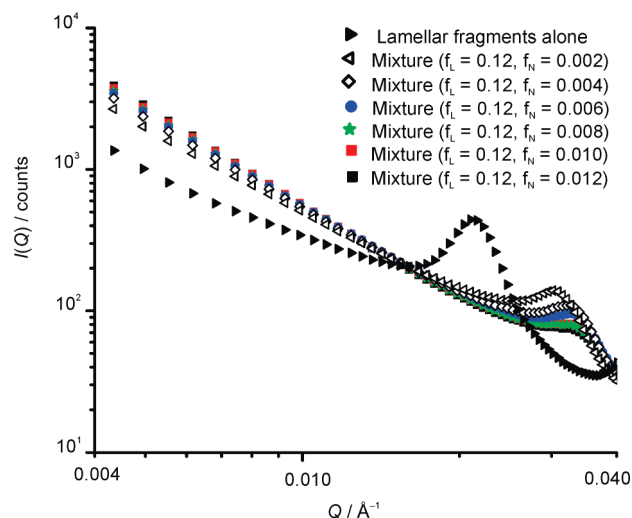


**Figure 1.** Small-angle neutron scattering data for lamellar fragments alone and mixtures of lamellar fragments and nickel hydroxide particles with varying composition. The data for static samples were collected using 1 mm thick quartz cells. The diffraction peak from the lamellar fragments moves toward higher  $Q$  with the addition of  $\text{Ni}(\text{OH})_2$  particles.  $f_L$  is the volume fraction of lamellar fragments, and  $f_N$  is the volume fraction of  $\text{Ni}(\text{OH})_2$  particles in the mixture.

calculated by taking an ensemble average of  $P_2$  using the angle,  $\Phi$ , between the unique axis of each particle (e.g., the axis of the cylinder) and the vector known as the director that lies in the principle direction of orientation provided by an external field. As the scattered intensity depends directly on the number of particles and their orientation, the order parameter,  $S_2$ , can be calculated from the anisotropy in the diffracted intensity<sup>31</sup> and from anisotropic small-angle scattering patterns<sup>40</sup> as described in previous articles. Explicitly,  $S_2$  is obtained from the distribution of scattered intensity,  $I(\Phi, Q)$ , as

$$S_2(Q) = \frac{\int_{\Phi=0}^{2\pi} \left\{ I(\Phi, Q) \times \frac{1}{2} [3 \cos^2(\Phi) - 1] \right\} d\Phi}{\int_{\Phi=0}^{2\pi} I(\Phi, Q) d\Phi} \quad (2)$$

where  $\Phi$  is the azimuthal angle between  $Q$  and the director. Integration is used to provide an appropriate average over all  $\Phi$  values from 0 to  $2\pi$ . The scattered intensity,  $I$ , arises from all of the particles sampled by the incident beam, and so, no further summation over the different particles is required. This procedure for calculation of an order parameter from scattering data is similar to that used in other studies.<sup>53</sup> The signal from the sample is much larger than the background scattering for the systems that are investigated, and corrections<sup>54</sup> for the background are negligible. If the platelets are randomly oriented, then the diffraction ring and the scattering patterns are isotropic and give the value of  $S_2 = 0.25$ . In considering the maximum orientation, it is useful to note that the Bragg peaks for a specific plane of a crystal of a perfectly aligned sample occur in a single direction, for which the maximum for  $S_2$  is 1, indicating complete orientational order. However, a lower maximum for  $S_2$  arises from the form factors of anisotropic particles that are measured in small-angle scattering. The intensity from perfectly aligned particles does not lie on a single line, and hence, the average  $S_2$  value will always be less than 1; this will be discussed further below. The extent of

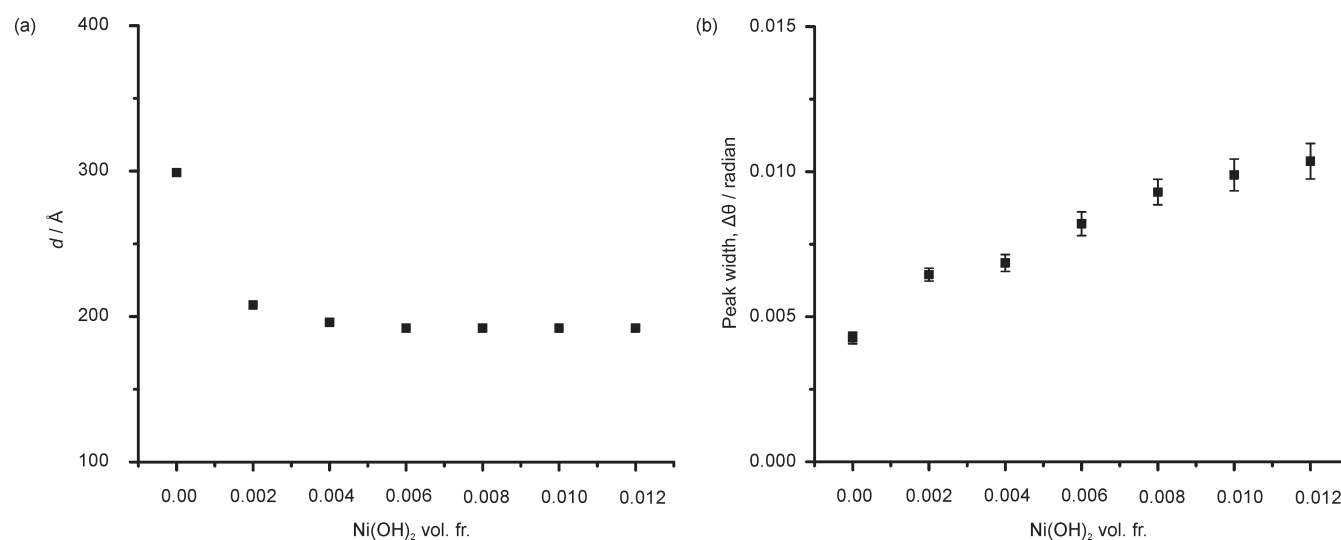


**Figure 2.** (a) Values of the lamellar spacing,  $d$ , obtained from the position of the peak in the scattering curves shown in Figure 1. The value of  $d$  decreases sharply with the addition of a small amount of  $\text{Ni}(\text{OH})_2$  particles and then remains almost constant. (b) Peak width as a function of  $\text{Ni}(\text{OH})_2$  particle concentration.

preferential alignment in the samples used in the current studies was quantified with the help of eq 2.

## RESULTS AND DISCUSSION

We divide our discussion into four parts. First, we discuss the effect of the  $\text{Ni}(\text{OH})_2$  particles on the lamellar fragments in static samples. Second, the behavior of lamellar fragments and the mixture under flow are discussed. In the third part, the orientational order in the mixture at different positions in the flow cell is discussed, and finally, the changes observed in the alignment of particles in a mixture along the extensional axis and at the inlet and the possible reasons for those changes are described.

**a. Effect of  $\text{Ni}(\text{OH})_2$  Particles on the Lamellar Fragments in Static Samples.** The lamellar fragments and mixtures with increasing concentration of  $\text{Ni}(\text{OH})_2$  particles measured at rest gave isotropic scattering patterns. The curves of scattered intensity are shown as functions of  $Q$  in Figure 1. Lamellar fragments show a strong Bragg peak from their internal structure. A small addition of  $\text{Ni}(\text{OH})_2$  particles (0.002 volume fraction) causes a large shift in the first Bragg peak characteristic of the lamellar phase to high  $Q$ . Further increases in the concentration of  $\text{Ni}(\text{OH})_2$  particles give smaller shifts to high  $Q$ , and the peak position becomes constant above 0.004 volume fraction of  $\text{Ni}(\text{OH})_2$  particles. A further noticeable feature is that the intensity of the peak drops upon addition of  $\text{Ni}(\text{OH})_2$  particles. The peak position in Figure 1 can be used to calculate the  $d$  spacing of the lamellar fragments. The calculated values of spacing,  $d$ , and the lamellar peak intensity are plotted against the volume fraction of  $\text{Ni}(\text{OH})_2$  particles in parts a and b, respectively, of Figure 2. The change in the  $d$  spacing and the width and visibility of the Bragg peak indicate changes in the structure of the lamellar fragments.

The sample with lamellar fragments alone has a spacing of  $d = 300$  Å, which decreases sharply to 190 Å upon addition of  $\text{Ni}(\text{OH})_2$  particles, as shown in Figure 2a. This demonstrates that a low concentration of the  $\text{Ni}(\text{OH})_2$  dispersion has a large effect on the  $d$  spacing of lamellar fragments. The spacing,  $d$ , remains unchanged for volume fractions,  $f_N$ , higher than 0.004.

The angular width,  $\Delta\theta$ , of the Bragg peak increases with  $\text{Ni}(\text{OH})_2$  particle concentration, as shown in Figure 2b. These changes could just be associated with the addition of the  $\text{Ni}(\text{OH})_2$  particles providing an additional screening that results in the reduction in the  $d$  spacing and a more flexible membrane, giving rise to the increased in the width of the Bragg peak. However, a more detailed analysis shows that there are other factors that are important. Hence, it is informative to calculate an approximate dimension,  $D$ , of the lamellar fragments in the direction perpendicular to the lamellae using the Debye–Scherrer formula<sup>55</sup>

$$D = \frac{0.9\lambda}{\cos \theta \Delta\theta} \quad (3)$$

where  $\theta$  is the scattering angle in radians.

The results of these calculations are presented in Table S2 in the Supporting Information and indicate that the size of the lamellar fragments changes from about 1300 to 500 Å. Thus, with a volume fraction of 0.012  $\text{Ni}(\text{OH})_2$  particles the number of repeating bilayers is, on average, only about two or three layers, decreased from just over four in the absence of  $\text{Ni}(\text{OH})_2$ . The addition of the particles apparently causes some delamination of the lamellar fragments, although the lateral dimension is still large and can not be determined directly from the scattering measurements. Further information about the mixture was obtained from a series of measurements made with different contrasts of the solvent ( $\text{H}_2\text{O}$  and  $\text{D}_2\text{O}$ ) for a sample with  $f_N = 0.012$  and  $f_L = 0.12$ . These are shown in the Supporting Information as Figure S3, and it is clear that the intensity of the Bragg peak disappears under conditions of the solvent matching the surfactant. This indicates that the  $\text{Ni}(\text{OH})_2$  particles do not form a regular structure.

The size of the particles is such that they are unlikely to penetrate between the individual bilayers of the lamellar fragments. This makes the system significantly different from those investigated in previous studies, such as laponite in the lamellar phase of nonionic surfactants, where fluctuation amplitudes of the surfactant layers are perturbed by thin rigid particles.<sup>56</sup> The indication of size from the Debye–Scherrer formula would be

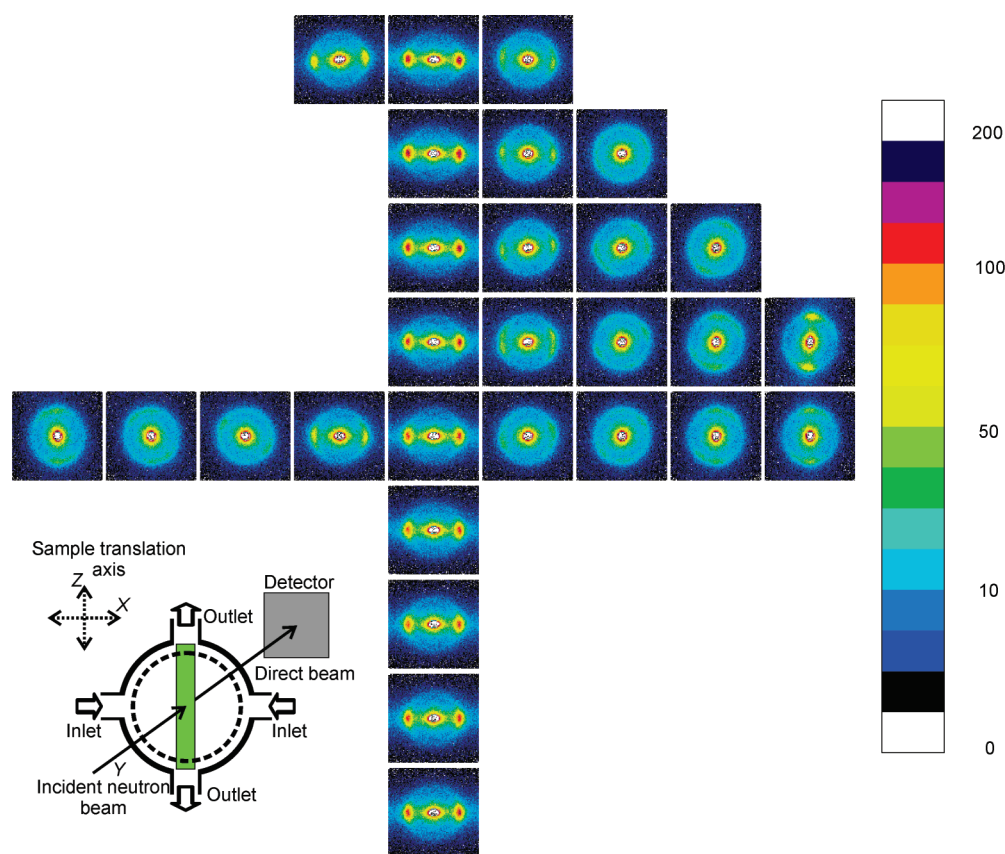


**Figure 3.** Small-angle neutron scattering measured at different positions within the cell window, as shown by the dashed circle in the inset, of the elongational flow pattern. The spatial separation of each scattering pattern is 2 mm in both the horizontal and vertical directions. Strong alignment of the pure lamellar fragments is observed in the extensional region at the flow rate of  $10 \text{ mL s}^{-1}$ . The position of the Bragg peak,  $Q$ , is the same as for the static sample of lamellar fragments.

modified if there were significant broadening of the Bragg peak from disorder or fluctuations of the lamellar structure. However, the loss of intensity seen in Figure 1 is consistent with delamination. The particles have an anionic stabilizer, which can interact with the cationic surfactant. The solubility of  $\text{Ni}(\text{OH})_2$  is very small,<sup>57</sup> but the addition of the dispersion does add some solvated ions to the dispersion of lamellar fragments that arise from both the dissociation of the  $\text{Ni}(\text{OH})_2$  particles and, more significantly, the stabilizer. This might screen electrostatic interactions and cause the decrease of the  $d$  spacing of the lamellar fragments. These ionic interactions are more likely to cause changes in lamellar structure than steric effects that would arise from depletion forces,<sup>42</sup> as the overall volume fraction of added particles was only just over 1%.

#### b. Lamellar Fragments and the Mixture in the Flow Cell.

Lamellar fragments and the mixture were measured at different flow rates in the elongational flow cell. The sample of lamellar fragment alone shows a strong Bragg peak from the internal structure of the particles that is particularly prominent under flow for the vertical line of maximum elongational strain rate in the raster map of scattering patterns shown in Figure 3. The Bragg peak is consistent with the position measured for the same sample at rest shown in Figure 2. The scattering patterns from the mixture, at all measured flow rates, do not show any sign of a Bragg peak. This applies for the scattering patterns in Figure 4 measured at a flow rate of  $7 \text{ mL s}^{-1}$  and for the other flow rates shown in Figure S1 in the Supporting Information. The absence

of the Bragg peak is witnessed even more clearly in the azimuthally averaged intensities obtained from the scattering patterns at the inlets and at the center of the cell that are plotted in Figure 8 (below). A curve that includes the scattering measured at larger  $Q$ , up to  $0.1 \text{ \AA}^{-1}$ , shown in Figure S4 in the Supporting Information confirms that the peak disappeared rather than simply moving outside the range of measurement. This absence of a diffraction peak suggests that the lamellar fragments in the mixture under flow no longer have a structure of repeating bilayers. This was not the case for the samples that were measured at rest, where the intensity decreased and the peak was noticeable for all compositions (see Figure 1). The combination of flow and addition of  $\text{Ni}(\text{OH})_2$  particles apparently causes further reduction of the internal structure and size of the lamellar fragments. Indeed, we postulate that the co-alignment of the  $\text{Ni}(\text{OH})_2$  platelets between aligned lamellar fragments exerts an additional force that promotes further delamination to the point where the number of bilayers per fragment is sufficiently small that a Bragg peak from the internal structure is no longer visible.

Some samples with different contrast were measured in an attempt to identify the structure of the individual components in the mixture under flow. However, as the samples measured at rest showed more internal structure than the lamellar fragment in the mixture measured under flow, it is difficult to use those data to model the structure under flow. For samples in  $\text{D}_2\text{O}$ , the scattering is dominated by the large lamellar fragments, and the signal from the small fraction of nickel hydroxide particles



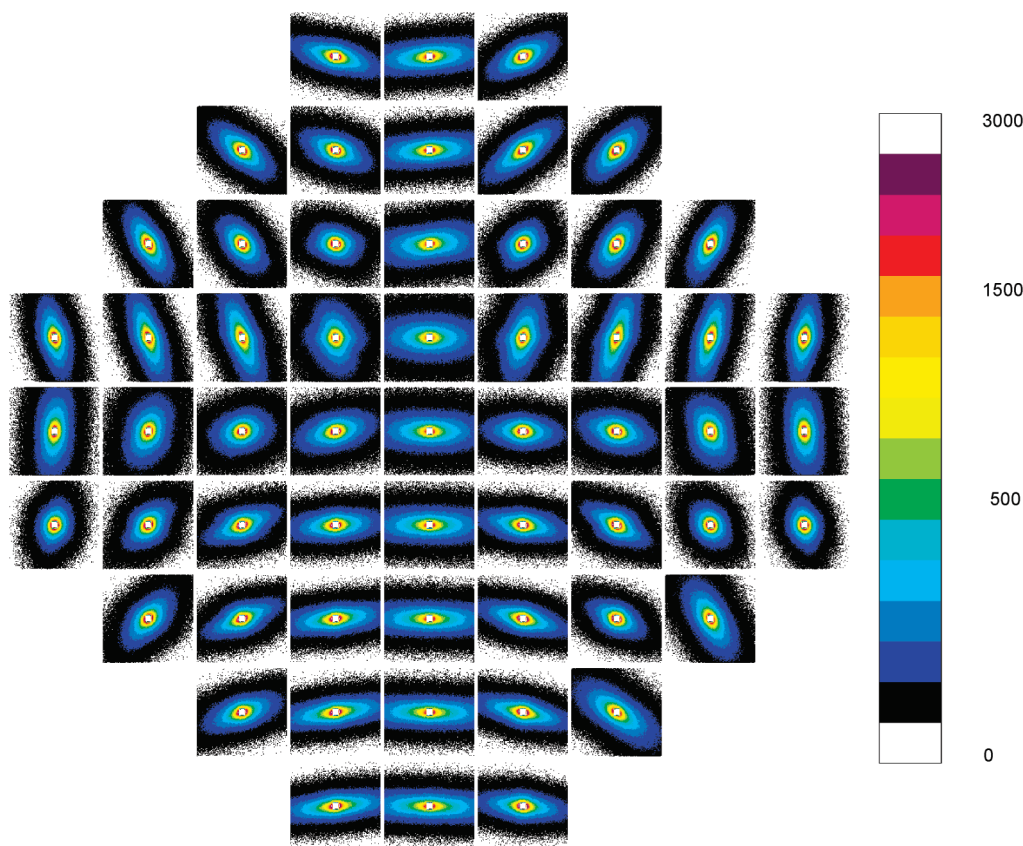


**Figure 4.** Scattering patterns for a mixture of lamellar fragments and  $\text{Ni}(\text{OH})_2$  particles at a flow rate of  $7 \text{ mL s}^{-1}$ . The spatial separation of each scattering pattern is 2 mm in both the horizontal and vertical directions. Data sets are anisotropic at most of the measured positions in the flow cell. Alignment is more pronounced along the vertical axis where the sample experiences the highest elongational strain rate. It is noticeable that the Bragg peak from the lamellae is not present in any of the patterns.

is not significant. The slopes of all of the curves, even at contrasts that are close to matching the surfactant, are consistent with large planar objects. This suggests association of the nickel hydroxide particles with the surfactant. It is therefore not appropriate to attempt to interpret the data measured with different contrasts as arising from separately distributed components.

**c. Spatial Variation of Alignment in the Flow Cell.** Scattering patterns for the circular window, along horizontal and vertical axes and in a quadrant, of the elongational flow cell for lamellar fragments are shown in Figure 3. The line through the center of the cell on the vertical ( $Z$ ) axis is the region with the highest elongational strain rate.

An increase in the anisotropy in the scattering patterns measured at the center of the cell with flow rate for the lamellar fragments was reported previously for a similar sample.<sup>33</sup> The present data are consistent with the previous measurements. The flow rate in the current studies was selected to be that at which there is maximum orientation. A strong diffraction peak from the highly aligned lamellar fragments is seen, and this intensity is constant for measurements at different positions along the vertical axis of the flow cell.

The full set of the scattering patterns obtained by the raster scan of the viewable circular window of the flow cell for the mixture at the lowest measured flow rate are shown in Figure 4. Scattering patterns from the mixture also exhibit strong anisotropy, especially in the region of maximum extension. The anisotropy decreases with increasing flow rate, and the effects

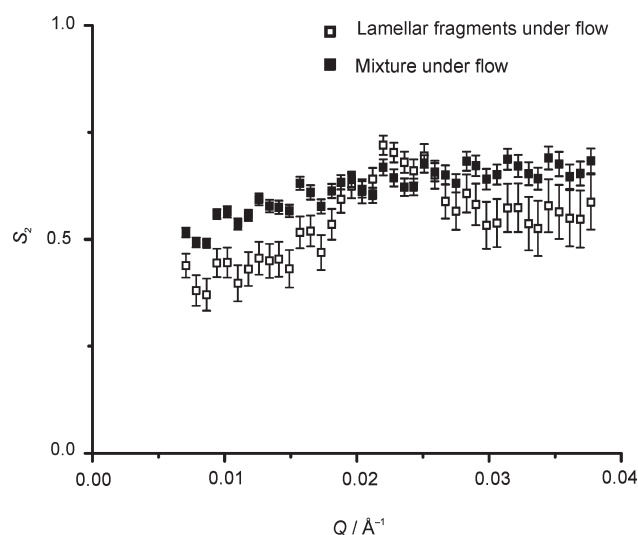


**Figure 5.**  $S_2$  as a function of  $Q$  for both the lamellar fragments alone and the mixture with particles. The value of  $S_2$  is higher at the Bragg peak for the lamellar fragments, and it shows a variation with  $Q$  for the mixture: it reaches a plateau at higher  $Q$ . These examples of calculations for  $S_2$  were taken for scattering patterns measured at the center of the cell.

are more prominent at the inlets, as shown in the scattering maps in Figure S1 in the Supporting Information. A decrease in the

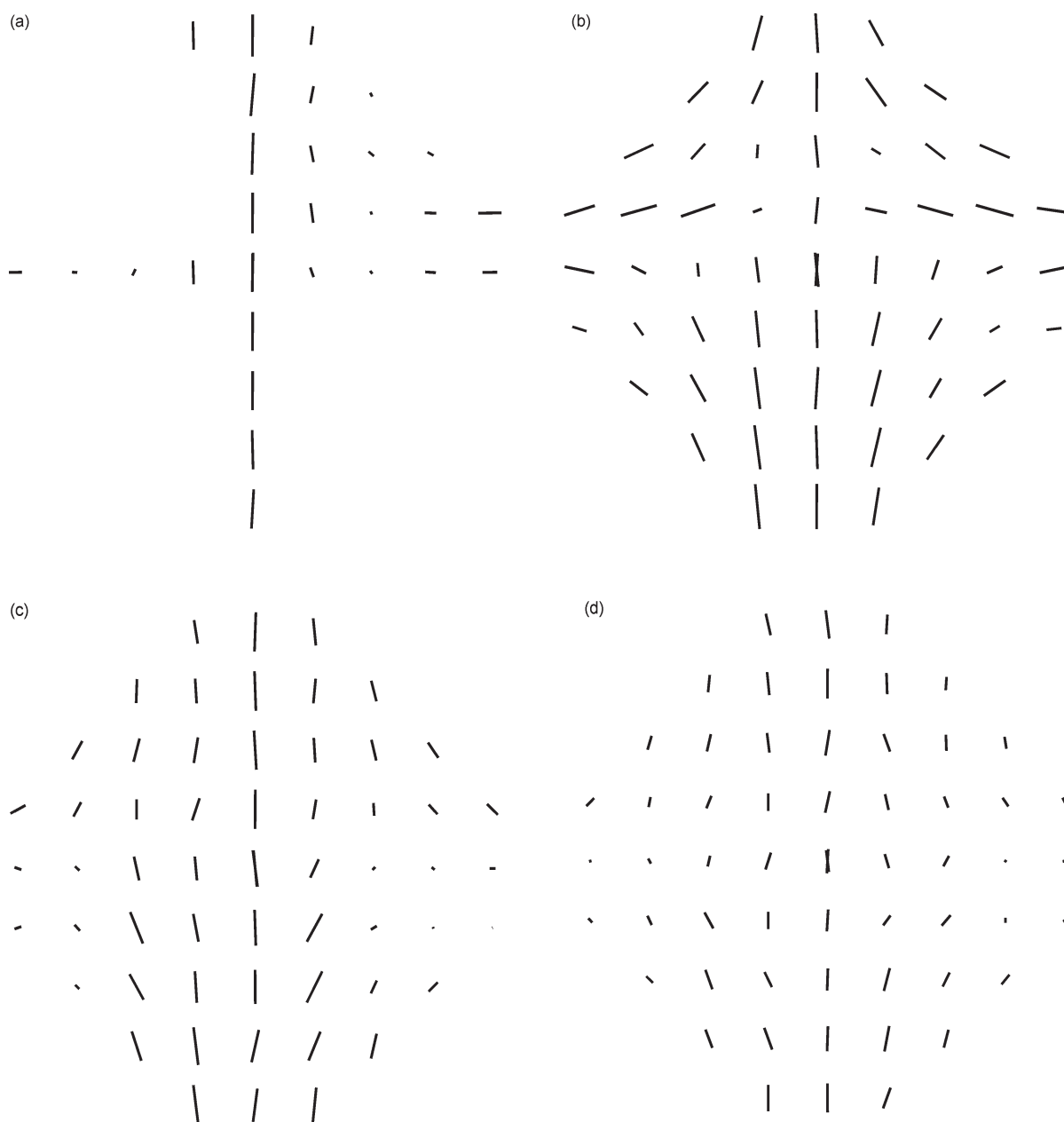


**Figure 6.** Values of  $S_2$  for (a) pure lamellar fragments and (b–d) a mixture of lamellar fragments and  $\text{Ni}(\text{OH})_2$  particles at (b) 7, (c) 13, and (d)  $28 \text{ mL s}^{-1}$ . The length of each line is the fractional difference of the maximum and minimum values of  $S_2$  for the flow. This represents the extent of orientation of those particles with their large faces parallel to the neutron beam. The direction is along the individual director of each data set, which is also the local flow direction. The small-angle neutron scattering patterns for the mixture at the flow rates shown in panels c and d are presented in the Supporting Information.

anisotropy under shear in a Couette cell at strain rates of  $500 \text{ s}^{-1}$  and above was reported for lamellar fragments<sup>33</sup> and attributed to a shear-induced lamellar to vesicle transition. In the elongational flow cell, the inlets and outlets are 7 mm long rectangular channels with a cross-sectional area of  $10 \times 6 \text{ mm}$ . The velocity of the sample has its maximum value at the inlets and outlets. This gives the highest shear strain rates,  $\dot{\gamma}_Y$ , in the direction of the beam at these positions. At the maximum flow rate of  $28 \text{ mL s}^{-1}$ ,  $\dot{\gamma}_Y$  is  $61 \text{ s}^{-1}$ . The shear gradients in the plane of the cell ( $XZ$  plane) are smaller, and at the highest flow rate, they have a magnitude of about  $14 \text{ s}^{-1}$ .

The observed decrease in the anisotropy with flow rate along the extensional axis is not the same as in our previous studies on

concentrated dispersions of  $\text{Ni}(\text{OH})_2$  particles<sup>40</sup> and lamellar fragments,<sup>33</sup> where the scattering patterns showed an increase in anisotropy arising from preferential alignment with their large face parallel to the incident beam with increases in flow rate.

As discussed above, the anisotropy in the scattering pattern gives a measure of alignment at the position of measurement in the flow cell. For the calculation of  $S_2$ , the director is defined as the local flow direction at each position in the flow cell.  $S_2$  is  $Q$ -dependent for both lamellar fragments and the mixture, as shown in Figure 5.

$S_2$  is higher at the Bragg peak in the sample that contains only lamellar fragments because the scattering arises predominantly



from the internal structure. The order parameters for the mixture also show some variation with  $Q$  that could arise if either the scattering objects are very anisotropic, not simply ellipsoids, or the scattering comes from separate components. However, the different contrasts used in scattering experiments suggest that the mixture does not consist of uncorrelated, independently scattering objects. Because of this  $Q$  dependence of  $S_2$  for the lamellar fragments alone, we selected a range at the Bragg peak of  $Q = 0.020\text{--}0.024\text{ \AA}^{-1}$  to calculate  $S_2$ . For the mixture with particles,  $S_2$  values were obtained from averages over the  $Q$  range from  $0.022$  to  $0.032\text{ \AA}^{-1}$  where there is a plateau and no further dependence on  $Q$ . The calculated values of  $S_2$  at  $Q$  values above

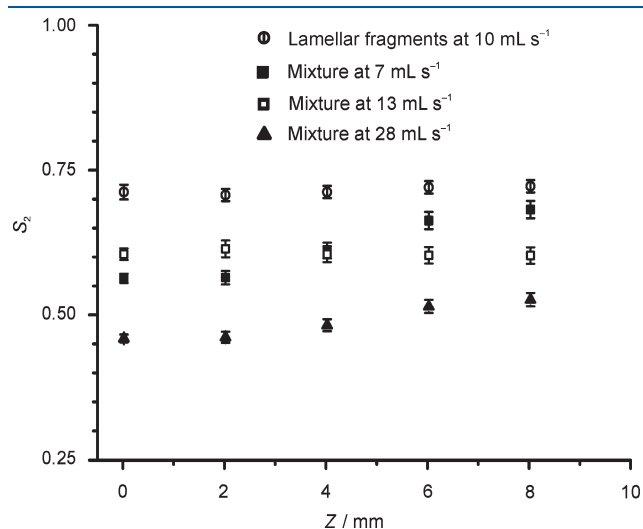
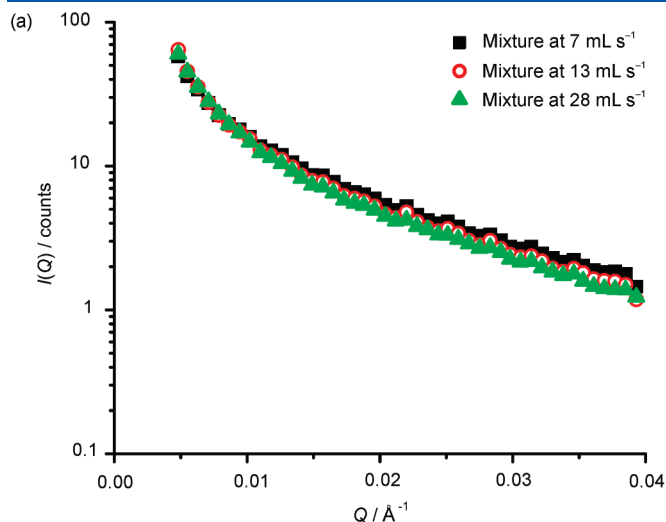


**Figure 7.** Values of the order parameter  $S_2$  calculated from the scattering patterns in the maps for the lamellar fragments and for the mixture of lamellar fragments and  $\text{Ni}(\text{OH})_2$  particles plotted against the position along the extensional axis in the elongational flow cell. Lamellar fragments alone display maximum alignment at the center of the cell, and this is unchanged along the extensional axis.  $S_2$  for the mixture shows differences with flow rate: At the lowest and highest measured flow rates,  $S_2$  increases from the cell center to the outlet, whereas the mixture at the intermediate flow rate shows little variation.



$0.032\text{ \AA}^{-1}$  for the mixture are shown in the Figure S5 in the Supporting Information. The scattering from cylinders and disks has been described by Pedersen,<sup>58</sup> and the value of  $S_2$  that would be obtained for a perfectly aligned sample can be estimated for a given  $Q$  value if the radius and thickness of the particle are known. The hydrodynamic radius of a platelike particle strongly depends on the long axis of the particle, and the relation is given by Mazer et al.<sup>59</sup> Thicknesses for the lamellar fragment particles of  $500\text{--}600\text{ \AA}$  are consistent with the observed anisotropy in the scattering, the weak appearance of a Bragg peak, and the constraint of a hydrodynamic radius  $R_h$  of  $1200\text{ \AA}$ . Although the sample with nickel hydroxide particles does not show a Bragg peak and so might be thinner, the light scattering suggests that the average diameter is about  $3000\text{ \AA}$ , and if the particles were much thinner than  $600\text{ \AA}$ , then it is unlikely that the scattering would be less anisotropic than for the lamellar fragments alone.

The estimated maximum value of  $S_2$  for particles with these dimensions is about  $0.78$ . The maximum value of  $S_2$  calculated from the experimental data for the lamellar fragments, at the diffraction peak, is  $0.72$ . The anisotropy, quantified in terms of  $S_2$ , for directors chosen to be along the local flow direction for each position is plotted for the lamellar fragments alone in Figure 6a and for the mixture at the three measured flow rates,  $7$ ,  $13$ , and  $28\text{ mL s}^{-1}$ , in parts b–d, respectively, of Figure 6.

Experimental data for the mixture of lamellar fragments and nickel hydroxide particles give a maximum of  $S_2$  of  $0.69$  and a minimum value of  $0.26$ . The minimum value of  $S_2$  for the lamellar fragments alone is  $\sim 0.28$ . The lengths of the lines in Figure 6 are proportional to the fractional differences between the measured maximum from the experimental data,  $0.72$ , and minimum,  $0.26$ , value of  $S_2$ . Comparison of the length of the lines at the inlets and along the extensional axis in Figure 6a shows that lamellar fragments are less aligned as they enter the cell at the inlets. There is maximum preferential alignment at the center of the cell after rotation of  $90^\circ$  for a given flow rate. The rotation is in the plane of the detector with respect to their orientation at the inlet. Lines of approximately the same length along the vertical axis show that the alignment of the lamellar fragments stays the same under extension, which was estimated to be  $6.2\text{ s}^{-1}$ . The mixture at the lowest given flow rate has comparatively higher alignment

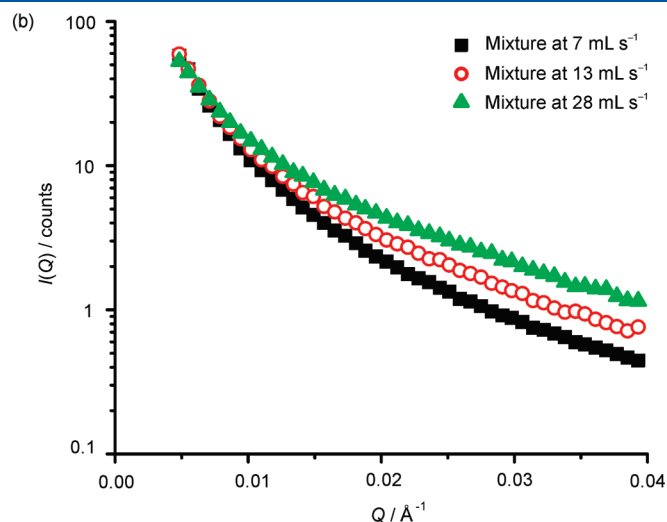


**Figure 8.** Azimuthally averaged scattered intensity from a mixture of lamellar fragments and  $\text{Ni}(\text{OH})_2$  particles at three flow rates for the (a) cell center and (b) inlet to the cell. In panel b, an increase in intensity at high  $Q$  with flow rate is observed. The Bragg peak from the internal structure of the lamellar fragments does not appear for the mixture of lamellar fragments and  $\text{Ni}(\text{OH})_2$  particles under flow at any measured position in the elongational flow cell.

at the inlet with respect to higher flow rates.  $S_2$  in the mixture decreases as the flow rate increases, as shown by the lengths of the lines in Figure 6b–d. This suggests that fewer particles are aligned with their large face parallel to the incident beam, and this reduces the anisotropy in the scattering patterns. Possible reasons for the decrease in the anisotropy with increasing flow rates are discussed in the next section.

**d. Changes in  $S_2$  along the Extensional Axis and Role of the Inlet.** As discussed earlier, the extensional strain rate for a given flow rate remains constant along the extensional ( $Z$ ) axis. The value of extensional strain rate for the lamellar fragments at  $10 \text{ mL s}^{-1}$  is  $6.2 \text{ s}^{-1}$ , and those for the mixture at the three measured flow rates of 7, 13, and  $28 \text{ mL s}^{-1}$  are estimated to be 4.2, 8.3, and  $17 \text{ s}^{-1}$ , respectively. Values of  $S_2$  along the extensional axis, for the lamellar fragments alone and for the mixture with particles at the three measured flow rates, are plotted in Figure 7 against the position of sample in the flow cell from the cell center to the outlet.

The values of  $S_2$  are higher for the lamellar fragments; they show maximum orientation at the center of the cell and remain the same along the extensional axis to the outlet. This trend is similar to that observed in the concentrated dispersions of  $\text{Ni}(\text{OH})_2$  particles on their own (0.07 volume fraction)<sup>40</sup> under higher extensional strain rates of about  $16 \text{ s}^{-1}$ . Although the volume fraction of lamellar fragments is higher than that of the  $\text{Ni}(\text{OH})_2$  particles in our previous studies, the larger particles are expected to align more strongly at lower strain rates. For the mixture at the lowest measured flow rate,  $S_2$  increases along the extensional axis from the cell center to the outlet. This trend is similar to that observed in the concentrated dispersion of  $\text{Ni}(\text{OH})_2$  particles at moderate flow rate. The data for the mixture measured at the highest flow rate exhibit a similar increase in  $S_2$  from the cell center to the outlet, as shown in Figure 7. At the intermediate flow rate, the mixture does not show changes in  $S_2$  along the extensional axis, and the trend is similar to that of the lamellar fragments alone. The average transit time for the particles in the elongational flow cell is about 1 s. This residence time is apparently not important for the lamellar fragments and for the mixture at intermediate flow rates, as the maximum order is already reached very close to the center of the cell.

Azimutally averaged, scattered intensities for the mixture for three measured flow rates are plotted against  $Q$  for scattering at the cell center and at the inlets in parts a and b, respectively, of Figure 8. The patterns are more anisotropic at the center, and the anisotropy decreases with increasing flow rate, as indicated by the lengths of the lines in Figure 6b–d. The azimuthally averaged intensities at the cell center for the three measured flow rates are similar, and the curves overlap. The overlap is significant, and it suggests that the change in anisotropy of scattering does not arise from the scattering objects tilting out of the vertical plane, but that they have an orientation distribution that is described only by the azimuthal angle,  $\Phi$ . The decrease in anisotropy at the higher flow rate could be associated with the significant decrease in viscosity that was observed. For a non-Newtonian fluid, such as that investigated here, further interpretation would require more detailed modeling to included materials properties that vary with strain rate.

In contrast, the scattering shown in Figure 8b increases with flow rate at high  $Q$ . These scattering patterns from the inlets correspond to regions where  $S_2$  decreases with flow rate. A decrease in anisotropy in the scattering from the mixture with

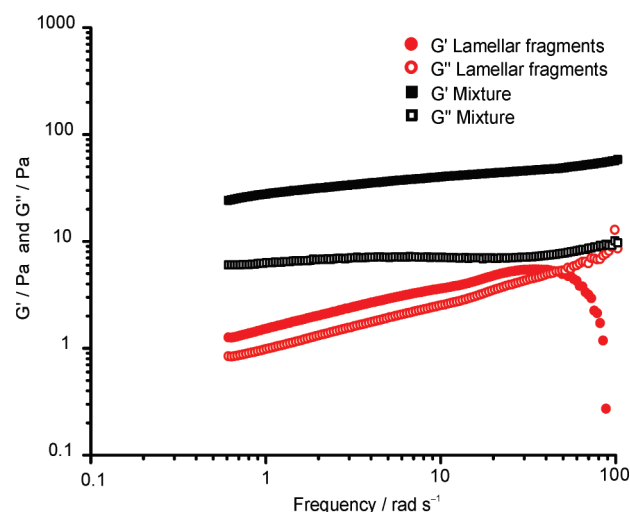


**Figure 9.** Storage modulus,  $G'$ , and loss modulus,  $G''$ , as functions of the angular frequency for lamellar fragments and the mixture. Higher values of the storage modulus for the mixture suggest strong interactions between the particles.

increasing flow rate suggests that the particles in the mixture are preferentially aligned with their large faces perpendicular to the incident beam at the inlets. This preferential alignment increases with flow rate, which reduces the anisotropy in the scattering patterns, but the azimuthally averaged scattering intensity increases at large  $Q$ . The convergence of all of the curves to similar values at low  $Q$  suggests that the particles in the mixture are not changing their size or state of aggregation either with increasing flow rate or at different positions in the cell. The observed changes in orientation with flow are consistent with the sample containing platelike objects rather than elongated micelles or spherical particles such as vesicles.

As discussed earlier, at the maximum flow rate ( $28 \text{ mL s}^{-1}$ ),  $\dot{\gamma}_Y$  is about  $61 \text{ s}^{-1}$ , and the shear gradients in the plane of the cell ( $XZ$  plane) have a magnitude of about  $14 \text{ s}^{-1}$ . These shear gradients increase with flow rate, increase the preferential alignment in particles in the mixture with their large faces perpendicular to the incident beam, and decrease the anisotropy in the scattering patterns.  $S_2$  decreases as the anisotropy decreases, as shown in Figure 6b–d. The effects are stronger at the inlets because the shear strain rates are higher and because the inlet is a rectangular cross-section pipe.

The cell geometry provides convergent flow toward the outlets. This rotates the large dimension of the particles toward the extensional axis and causes preferential alignment with their large faces parallel to the incident neutron beam. The effects of the convergent flow in the plane of the cell seem to be dominant over the shear strain rate in the beam direction at the outlets, as shown by the values of  $S_2$  in Figure 6b–d. The alignment is higher for a given flow rate at the outlets and on the vertical axis as compared to that at the inlets. It is interesting to consider the data for the alignment together with the rheological data for these samples shown in Figure 9. The dynamic viscosity calculated from these data are shown in Figure S6 in the Supporting Information. The storage modulus is much higher for the sample with the added nickel hydroxide particles, and this would support the idea of stronger interactions between the particles in this system that are disrupted by elongational strain. The shear strain rates in the flow cell are lower than those required for significant shear thinning.

These results show that the extensional strain rate of about  $6 \text{ s}^{-1}$  effectively induces high alignment of the particles, whereas a shear strain rate of about  $4000 \text{ s}^{-1}$  in a pipe flow exhibits such alignment only near the wall for clay particles with a similar size range.<sup>31</sup>

## CONCLUSIONS

We have studied the effect of the addition of  $\text{Ni}(\text{OH})_2$  particles on the rheological behavior of dispersions of lamellar fragments of cationic/nonionic surfactants. The samples have been studied by small-angle neutron scattering both at rest and under elongational flow. A small amount of  $\text{Ni}(\text{OH})_2$  particles was found to have a large effect on the behavior of lamellar fragments dispersed at 12% by volume: The viscosity was observed to be 7 times higher in the presence of  $\text{Ni}(\text{OH})_2$  particles at a volume fraction of 0.012, and the mixture behaved like a soft solid after storage for six months.

Rheological measurements indicate that the dynamic viscosity of both the lamellar fragments alone and the mixture of lamellar fragments and  $\text{Ni}(\text{OH})_2$  displays shear thinning and overlap each other at high shear rates. The spacing,  $d$ , of the lamellar phase decreases sharply with a small addition of  $\text{Ni}(\text{OH})_2$  particles in the mixtures at rest and then stays constant. The lamellar fragments retain some of their internal structure in the mixtures at rest, although the visibility of the Bragg peak diminishes. However, in the mixture studied under flow, the internal structure of the lamellar fragments is completely lost. Despite this loss of internal structure, the scattering experiments show that the mixture still consists of large anisotropic particles. The combined effects of the flow and the addition of particles causes delamination beyond that seen at rest. This suggests that the alignment promotes the interaction of the two components that drives the delamination.

The results demonstrate that very low extension strain rates effectively induce a high degree of alignment for the large lamellar fragments, in contrast to very high shear rates that are required for such alignment for similar-sized particles. Preferential alignment of the particles in the mixture with their large face perpendicular to the incident beam increases with flow rate as the shear gradients in the plane of the cell increase. The decrease in  $S_2$  and the increase in the azimuthally averaged scattered intensity at the inlet with flow rate in the mixture are attributed to the onset of an increase in preferential alignment, with large faces perpendicular to the beam, under pipe flow at the inlets. The effects of convergent flow are higher along the extensional axis, and this keeps the particles aligned at higher flow rates with their large face parallel to the incident neutron beam.

## ASSOCIATED CONTENT

**S Supporting Information.** Scattering patterns at the flow rates of 13 and  $28 \text{ mL s}^{-1}$  for the mixture 0.12 volume fraction lamellar fragments and 0.012 volume fraction  $\text{Ni}(\text{OH})_2$  (Figure S1), calculations using the Debye–Scherrer formula (Table S2), data from different contrast of mixtures (Figure S3), azimuthally averaged ( $0^\circ \pm 30^\circ$ ) intensity for the mixtures under flow at high  $Q$  (Figure S4), order parameter  $S_2$  for data over a wide range of  $Q$  values for the mixture at the lowest flow rate (Figure S5), and rheological data from lamellar fragments alone and the mixture (Figure S6). This information is available free of charge via the Internet at <http://pubs.acs.org>.

## AUTHOR INFORMATION

### Corresponding Author

\*Tel.: +46 18 471 3522. Fax: +46 18 471 3524. E-mail: Junaid.Qazi@fysik.uu.se.

### Notes

<sup>†</sup>On study leave from COMSATS Institute of Information Technology, Islamabad, Pakistan.

## ACKNOWLEDGMENT

We are grateful to the Institut Laue Langevin for the allocation of beam time and to Peter Cross, David Bowyer, and Steven Rowe for technical support in preparing the SANS measurements. Lionel Porcar and Ida Berts are thanked for collecting the scattering data for the samples measured at rest. This work was supported, in part, by the Swedish Research Council (VR).

## REFERENCES

- (1) Janek, M.; Lagaly, G. *Colloid Polym. Sci.* **2003**, *281*, 293–301.
- (2) Manski, J. M.; van der Goot, A. J.; Boom, R. M. *Trends Food Sci. Technol.* **2007**, *18*, 546–557.
- (3) Walkenström, P.; Hermansson, A. M. *Curr. Opin. Colloid Interface Sci.* **2002**, *7*, 413–418.
- (4) Barnes, H. A.; Hutton, J. F.; Walters, K. *An Introduction to Rheology*; Elsevier: Amsterdam, 1985.
- (5) Goodwin, J. W.; Hughes, R. W. *Rheology for Chemists: An Introduction*; Royal Society of Chemistry: Cambridge, U.K., 2000.
- (6) Berni, M. G.; Lawrence, C. J.; Machin, D. *Adv. Colloid Interface Sci.* **2002**, *98*, 217–243.
- (7) Clarke, S. M.; Rennie, A. R.; Ottewill, R. H. *Adv. Colloid Interface Sci.* **1995**, *60*, 95–118.
- (8) Ottewill, R. H.; Johnson, G. D. W.; Rennie, A. R. *Adv. Colloid Interface Sci.* **2003**, *100–102*, 585–611.
- (9) Vermant, J.; Solomon, M. J. *J. Phys.: Condens. Matter* **2005**, *17*, R187–R216.
- (10) Ramsay, J. D. F.; Lindner, P. J. *Chem. Soc., Faraday Trans* **1993**, *89*, 4207–4214.
- (11) Brown, A. B. D.; Rennie, A. R. *Phys. Rev. E* **2000**, *62*, 851–862.
- (12) Melrose, J. R.; Ball, R. C. *J. Rheol.* **2004**, *937–960*.
- (13) Brunn, P. J. *Fluid Mech.* **1977**, *82*, 529–547.
- (14) Brunn, P. J. *Non-Newtonian Fluid Mech.* **1980**, *5*, 271–288.
- (15) Gauthier, F.; Goldsmith, H. L.; Mason, S. G. *Rheol. Acta* **1971**, *10*, 344–364.
- (16) Gunes, D. Z.; Scirocco, R.; Mewis, J.; Vermant, J. *Non-Newtonian Fluid Mech.* **2008**, *155*, 39–50.
- (17) Mewis, J.; Metzner, A. B. *J. Fluid Mech.* **1974**, *62*, 593–600.
- (18) Binks, B. P.; Rodrigues, J. A. *Langmuir* **2007**, *23*, 3626–3636.
- (19) Mulqueen, P. *Adv. Colloid Interface Sci.* **2003**, *106*, 83–107.
- (20) Lekkerkerker, H. N. W.; Poon, W. C. K.; Pusey, P. N.; Stroobants, A.; Warren, P. B. *Europhys. Lett.* **1992**, *20*, 559–564.
- (21) Laurati, M.; Petekidis, G.; Koumakis, N.; Cardinaux, F.; Schofield, A. B.; Brader, J. M.; Fuchs, M.; Egelhaaf, S. U. *J. Chem. Phys.* **2009**, *130*, 134907(1)–134907(14).
- (22) Sedgwick, H.; Egelhaaf, S. U.; Poon, W. C. K. *J. Phys.: Condens. Matter* **2004**, *16*, S4913–S4922.
- (23) Strivens, T. A. *Colloid Polym. Sci.* **1989**, *267*, 769–780.
- (24) George, J.; Sudheesh, P.; Reddy, P. N.; Sreejith, L. J. *Solution Chem.* **2009**, *38*, 373–381.
- (25) Lu, T.; Huang, J.; Li, Z.; Jia, S.; Fu, H. *J. Phys. Chem. B* **2008**, *112*, 2909–2914.
- (26) Raghavan, S. R.; Kaler, E. W. *Langmuir* **2001**, *17*, 300–306.
- (27) Lin, Y.; Han, X.; Cheng, X.; Huang, J.; Liang, D.; Yu, C. *Langmuir* **2008**, *24*, 13918–13924.



- (28) Soubiran, L.; Staples, E.; Tucker, I.; Penfold, J.; Creeth, A. *Langmuir* **2001**, *17*, 7988–7994.
- (29) Rennie, A.; Bare, S.; Cockcroft, J. K.; Jupe, A.; C. J. *Colloid Interface Sci.* **2006**, *293*, 475–482.
- (30) Bare, S.; Rennie, A. R.; Cockcroft, J. K.; Colston, S. L.; Jupe, A. C. J. *Appl. Crystallogr.* **2001**, *34*, 573–579.
- (31) Qazi, S. J. S.; Rennie, A. R.; Wright, J. P.; Cockcroft, J. K. *Langmuir* **2010**, *26*, 18701–18709.
- (32) Penfold, J.; Staples, E.; Tucker, I.; Carroll, P.; Clayton, J.; Cowan, J. S.; Lawton, G.; Amin, S.; Ferrante, A.; Ruddock, H. J. *Phys. Chem. B* **2006**, *110*, 1073–1082.
- (33) Penfold, J.; Tucker, I. J. *Phys. Chem. B* **2007**, *111*, 9496–9503.
- (34) Ramos, L.; Fabre, P.; Dubois, E. J. *Phys. Chem.* **1996**, *100*, 4533–4537.
- (35) Ponsinet, V.; Fabre, P. J. *Phys. Chem.* **1996**, *100*, 5035–5038.
- (36) Salamat, G.; Kaler, E. W. *Langmuir* **1999**, *15*, 5414–5421.
- (37) Nettesheim, F.; Grillo, I.; Lindner, P.; Richtering, W. *Langmuir* **2004**, *20*, 3947–3953.
- (38) Imai, M.; Mawatari, R.; Nakaya, K.; Komura, S. *Eur. Phys. J. E* **2004**, *13*, 391–400.
- (39) Wang, N.; Liu, S.; Zhang, J.; Wu, Z.; Chen, J.; Sun, D. *Soft Matter* **2005**, *1*, 428–430.
- (40) Qazi, S. J. S.; Rennie, A. R.; Tucker, I.; Penfold, J.; Grillo, I. J. *Phys. Chem. B* **2011**, *115*, 3271–3280.
- (41) Scheuermann, R.; Tucker, I. M.; Creeth, A. M.; Dilger, H.; Beck, B.; Roduner, E. *Phys. Chem. Chem. Phys.* **2002**, *4*, 1510–1512.
- (42) Penfold, J.; Staples, E.; Ugazio, S.; Tucker, I.; Soubiran, L.; Hubbard, J.; Noro, M.; O'Malley, B.; Ferrante, A.; Ford, G.; Buron, H. J. *Phys. Chem. B* **2005**, *109*, 18107–18116.
- (43) Brown, A. B. D.; Clarke, S. M.; Rennie, A. R. *Langmuir* **1998**, *14*, 3129–3132. *Langmuir* **1999**, *15*, 1594.
- (44) Durand-Keklikian, L.; Haq, I.; Matijevic, E. *Colloids Surf. A* **1994**, *92*, 267–275.
- (45) Qazi, S. J. S.; Rennie, A. R.; Cockcroft, J. K.; Vickers, M. J. *Colloid Interface Sci.* **2009**, *338*, 105–110.
- (46) Rehage, H.; Hoffmann, H. *Mol. Phys.* **1991**, *74*, 933–973.
- (47) Idziak, S. H. J.; Welch, S. E.; Kisilak, M.; Mugford, C.; Potvin, G.; Veldhuis, L.; Sirota, E. B. *Eur. Phys. E* **2001**, *6*, 139–145.
- (48) COMSOL Multiphysics, version 3.5a; COMSOL, Inc.: Burlington, MA, November, 2008; www.comsol.com.
- (49) Meng, Q. J.; Higdon, J. J. L. *J. Rheol.* **2008**, *52*, 37–65.
- (50) Fuller, G. G.; Cathey, C. A.; Hubbard, B.; Zebrowski, B. E. *J. Rheol.* **1987**, *31*, 235–249.
- (51) Clarke, S. M.; Rennie, A. R.; Convert, P. *Europhys. Lett.* **1996**, *35*, 233–238.
- (52) Spiegel, M. R. *Mathematical Handbook of Formulas and Tables*; McGraw-Hill: New York, 1968; p 146.
- (53) Deutsch, M. *Phys. Rev. A* **1991**, *44*, 8264–8270.
- (54) Hoekstra, H.; Vermant, J.; Mewis, J. *Langmuir* **2002**, *18*, 5695–5703.
- (55) Scherrer, P. *Nachr. Ges. Wiss. Göttingen, Math.–Phys. Kl.* **1918**, *26*, 98 (in German).
- (56) Grillo, I.; Levitz, P.; Zemb, T. *Eur. Phys. J. E* **2001**, *5*, 377–386.
- (57) Gayer, K. H.; Garrett, A. B. J. *Am. Chem. Soc.* **1949**, *71*, 2973–2975.
- (58) Pedersen, J. S. *Adv. Colloid Interf. Sci.* **1997**, *70*, 171–210.
- (59) Mazer, N. A.; Benedek, G. B.; Carey, M. C. *Biochemistry* **1980**, *19*, 601–615.